ACS OMEGA

http://pubs.acs.org/journal/acsodf

Article

Magnetic, Electronic, and Mechanical Properties of Bulk ε-Fe_2N Synthesized at High Pressures

Teng Ma, Yunyu Yin, Fang Hong,* Pinwen Zhu,* and Xiaohui Yu*

Cite This: *ACS Omega* 2021, 6, 12591−12597

Read Online

ACCESS | Metrics & More | Article Recommendations | Supporting Information

ABSTRACT: We sintered bulk trigonal ε-Fe_2N (space group: $P\bar{3}12$) with the high-pressure and high-temperature method. Structural refinements by the Rietveld method result in a trigonal unit cell with parameters of a = 4.7767(1) Å and c = 4.4179(3) Å. ε-Fe_2N is ferromagnetic with a Curie temperature of ∼250 K, a saturation magnetization (M_s) value of up to 1.2 μ_B/formula units (f.u.), and comparatively low coercive field. The Vickers hardness was measured, and the results showed that the asymptotic hardness of bulk ε-Fe_2N is about 6.5 GPa with a load of 1000 g. Thermogravimetric (TG) analysis shows that ε-Fe_2N is thermally stable below 670 K. ε-Fe_2N exhibits good metal conductivity, and the electron transport measurements show that the resistivity of it is 172 $\mu\Omega$ cm at room temperature. The theoretical calculations suggest that the conducting states are mainly derive from Fe-3d states.

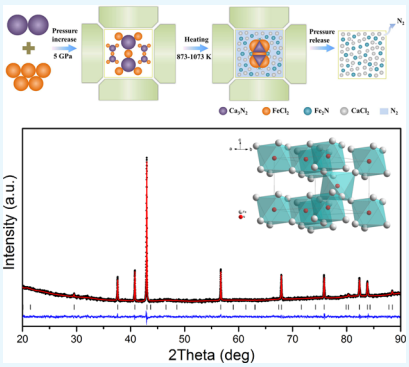

INTRODUCTION

Transition-metal nitrides are fascinating materials and have attracted considerable attention for their fundamental properties, technological applications in high-energy-density materials, high hardness, high refractory, and catalytic properties.[1−8] Because of steel production and steel hardening, iron nitrides have been thoroughly investigated since the beginning of the last century.[9,10] There are several known compounds in the Fe−N system, such as tetragonal α''-$Fe_{16}N_2$,[11] tetragonal α'-Fe_8N,[12] cubic γ'-Fe_4N,[13] hexagonal ε-Fe_3N,[14] hexagonal β-Fe_7N_3,[15] orthorhombic ζ-Fe_2N,[16,17] Fe_3N_2,[18] cubic FeN,[19−22] marcasite FeN_2,[23] and triclinic FeN_4.[18] Early metal nitrides were synthesized by a reaction of metal with N_2 or NH_3 gas.[19,24] As the research progresses, metal nitrides have also been prepared from metal halides, metal oxides with nitrogen or ammonia precursors.[25−30] So far, nitrogen and ammonia as nitrogen sources are still the main route to synthesize metal nitrides. In the 1990s, the reactive solid nitrogen sources, such as Li_3N and NaN_3, were used as precursors of the solid-state metathesis (SSM) reaction to prepare metal nitrides.[31−34] Despite the increasing variety of metal nitride synthesis methods, the preparation of bulk iron nitride remains a challenge due to the fact that iron nitrides are a thermally metastable material that can easily decompose and lose nitrogen under high-temperature conditions. Up to now, synthetic products of iron nitrides are still concentrated in nanomaterials, microcrystalline materials, and thin-film materials. Niewa et al. used microcrystalline ε-Fe_3N as the precursor to sinter bulk ε-Fe_3N by means of the high-temperature and high-pressure method.[35] Yin et al. reported the direct preparation of bulk ε-Fe_3N with hBN and alkaline metal ferrite or alkaline-earth metal ferrite at 5 GPa and 1627 K over 1−10 min by the SSM reaction.[36] Schwarz et al. reported that ε-$Fe_3N_{1.5}$ was obtained by phase transformation of ζ-Fe_2N.[37] Lehmann et al. reported that ε-$Fe_3N_{1.51}$ was synthesized electrochemically in a molten salt system KCl−LiCl at 723 K.[38] There are few reports that large-size bulk iron nitrides with a higher nitrogen content than Fe_3N were prepared and characterized. In this paper, we report the preparation of bulk ε-Fe_2N obtained at 8 GPa and 1273 K and characterize the properties of it. The magnetic properties, electrical properties, thermodynamic stability, and hardness have been measured in this work, and the electronic structures of ε-Fe_2N were investigated using the first-principles calculations.

RESULTS AND DISCUSSION

The ε-Fe_2N was prepared by the solid-state metathesis (SSM) reactions under high pressures and high temperatures between $FeCl_2$ and Ca_3N_2. The powder X-ray diffraction (XRD) patterns of washed products measured in ambient conditions are shown in Figure 1a. Under the condition that $Ca_3N_2/FeCl_2$ is 1:4 and the target temperature is 1273 K, the phase of ε-Fe_2N appears in the synthetic product. At other temperatures, the X-ray diffraction peak of the product is very poor. We attempted to increase the content of Ca_3N_2 and change the

Received: January 30, 2021
Accepted: April 21, 2021
Published: May 8, 2021

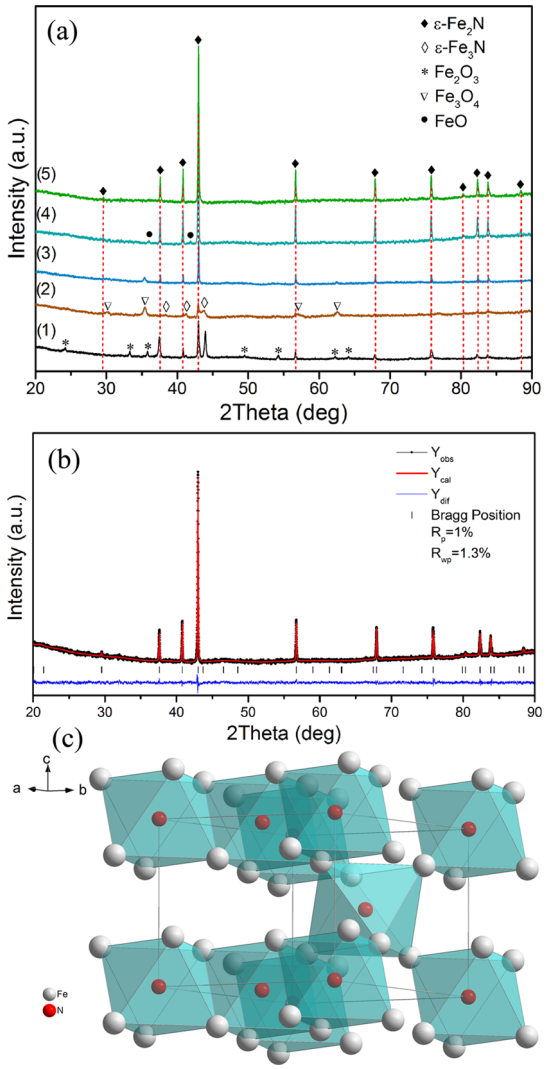

Figure 1. (a) X-ray diffraction patterns of samples under different preparation conditions: (1) $Ca_3N_2/FeCl_2$ = 1:4, 1273 K, 15 min. (2) $Ca_3N_2/FeCl_2$ = 1:3, 1273 K, 15 min. (3) $Ca_3N_2/FeCl_2$ = 1:3, 1073 K, 15 min. (4) $Ca_3N_2/FeCl_2$ = 1:2.8, 1073 K, 30 min. (5) $Ca_3N_2/FeCl_2$ = 1:2.5, 1073 K, 30 min. The XRD pattern of (5) is that of pure phase. (b) X-ray diffraction pattern and the result of Rietveld refinement with ε-Fe_2N. Observed (Solid dots), calculated (red line), the difference (blue line), and Bragg position (black vertical line) are displayed in the patterns. (c) Crystal structure of ε-Fe_2N.

target temperature to inhibit the appearance of iron oxides and ε-Fe_3N. When the content of Ca_3N_2 increases to $Ca_3N_2/FeCl_2$ =1:3 and the target temperature decreases to 1073 K, the phase of ε-Fe_3N disappears and the phase of iron oxide becomes Fe_3O_4. On further increasing the content of Ca_3N_2 until the ratio of $Ca_3N_2/FeCl_2$ is 1:2.5, the pure phase of ε-Fe_2N is obtained. In fact, according to the chemical reaction equation, Ca_3N_2 is excessive. This suggests that excessive Ca_3N_2 can inhibit the production of iron oxides.

The X-ray diffraction patterns and the result of Rietveld refinement are displayed in Figure 1b. The X-ray diffraction pattern of the compound is consistent with the standard card of ε-Fe_2N, without any additional diffraction peaks. There are two symmetries of ε-Fe_2N, trigonal $P312$ and hexagonal $P6_322$,[6,35,37−40] and the positions of the diffraction peaks of these two symmetries are consistent. In the structure of ε-Fe_2N, the structure of the iron atom is basically the same, and the nitrogen atom forms NFe_6 octahedron with the iron atom as the interstitial atom. The difference is the site of nitrogen atoms. For hexagonal $P6_322$ ε-Fe_2N, there are the 2b, 2c, and 2d crystallographic sites, which can be occupied by nitrogen atoms.[41] The octahedra of Fe_6 only share the corner at 2c sites; hence, the N−N distance is maximum, which minimizes the repulsion between the nitrogen atoms. The 2c sites can accommodate up to 25% nitrogen content. The 2b octahedra share edges with the populated 2c octahedra, and the 2d octahedra share faces with the populated 2c octahedra; hence, as the nitrogen content is increased, the next preferable octahedral interstitial site is the 2b sites. However, the octahedra at 2b sites share faces with each other, which requires that the nitrogen atoms occupying 2b sites are arranged alternatively to reduce the repulsion between the nitrogen atoms. Therefore, it is generally believed that the 2b site cannot be occupied by more than 50%. Therefore, in the structure of ε-Fe_2N as reported in the literature, the occupation of site 2c is close to 100%, and the occupation of site 2b is close to 50%. In the structure of ε-Fe_2N with a $P312$ symmetry, there are six crystallographic sites for nitrogen atoms, namely, 1a, 1b, 1c, 1d, 1e, and 1f.[41] However, due to the repulsion between nitrogen atoms,[42] nitrogen atoms can only occupy three interstitial sites, which are 1a, 1d, and 1e, respectively, and the occupation of sites 1a, 1d, and 1e is close to 100%. In this paper, structural refinements of the specimen ε-Fe_2N based on X-ray diffraction data were performed in both considered structure models in $P312$ and $P6_322$. The refined structural parameters of $P312$ and $P6_322$ are listed in Tables 1 and S1, respectively. Nitrogen atom occupations reported are N1 2c 0.993(4) and N2 2b 0.479(7) in Schwarz et al.[37] and N1 2b 0.606(7) and N2 2c 0.900(4) in Lehmann et al.[38] In our refinement, the occupation of nitrogen atoms of the two sites was basically the same, N1 2b 0.716(1) and N2 2c 0.772(1). Therefore, the $P312$ model is more consistent with our results. The results of Rietveld refinement show that the atomic ratio of Fe to N is 2.04:1. The approximate atomic ratio of Fe to N is 2:1.

Table 1. Crystallographic Parameters of ε-Fe_2N Obtained from the Rietveld Refinement

identification code			Fe_2N	
formula weight (g/mol)			62.7	
formula sum			FeN0.49	
formula unit, Z			6	
wavelength (Å)			1.5406	
crystal system			trigonal	
space group			$P312$ (no.149)	
unit cell dimensions (Å)			a = 4.7767(1) Å	
			c = 4.4179(3) Å	
volume (Å^3)			87.3 Å^3	
Θ range (deg)			20−90	
residuals			R_p = 1%	
			R_{wp} = 1.3%	
			χ^2 = 1.092	
atom	Wyckoff	(x, y, z)	occupancy	B (Å^2)
Fe	6l	0, 2/3, 1/4	1	0.556(7)
N1	1e	2/3, 1/3, 0	0.985(3)	0.486(2)
N2	1d	1/3, 2/3, 1/2	0.961(2)	0.649(2)
N3	1a	0, 0, 0	0.973(2)	0.533(1)

https://doi.org/10.1021/acsomega.1c00551
ACS Omega 2021, 6, 12591−12597

To investigate the thermal stability of ε-Fe_2N, thermogravimetric (TG) analysis and differential thermal analysis (DTA) were performed on the powder sample. The mixture of hydrogen (4%) and argon (96%) was used as a protective gas to prevent the sample from being oxidized. Above 670 K, the weight of the sample starts to decrease quickly, suggesting the occurrence of a decomposition reaction. At 940 K, ε-Fe_2N is completely decomposed into Fe. The measurement results are shown in Figure 2. The TG analysis gives a near nitrogen

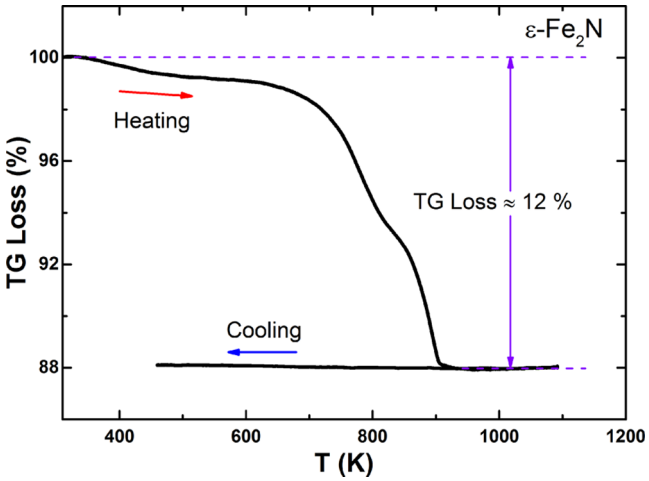

Figure 2. Temperature dependence of thermogravimetric (TG) loss for ε-Fe_2N.

stoichiometry (1.86). This result is consistent with the previous result of Rietveld refinement. In the Fe−N system, the decomposition temperature of the compound decreases with the increase of the nitrogen content. The decomposition temperature of ε-Fe_3N is reported to be 770 K.[36] Jiang et al. reported that the decomposition of the γ'-Fe_4N began at 910 K.[43] In this paper, the DTA of ε-Fe_2N showed the same heat flux peak as that reported in previous reports at the same temperature. The DTA of ε-Fe_2N is shown in Figure S1. This suggests that denitrogen of ε-Fe_2N is actually a phase-change process, from a high nitrogen phase to a low nitrogen phase, which is eventually completely decomposed into a single iron. The decomposition measurements of ε-Fe_2N were performed at 773 and 813 K. The results are shown in Figure S2. At 773 K, ε-Fe_2N was decomposed into Fe_3N and Fe_4N. At 813 K, ε-Fe_2N was decomposed into Fe_4N. The results demonstrate that the conjecture is correct.

The water-washed high-pressure product was tried to sinter at 5 GPa and 1073 K, but the attempt failed. The result of TG analysis experimentally demonstrates the thermal stability of ε-Fe_2N. The low decomposition temperature is one of the reasons why the powder of ε-Fe_2N is difficult to sinter into bulk materials under the same pressure and same temperature conditions, which are the preparation conditions of ε-Fe_2N. ε-Fe_2N can be synthesized without denitrogenation not only because of the presence of high pressure but also because the SSM reaction actually occurred under a condition of excessive nitrogen. Therefore, there are two options to inhibit the denitrogenation of the sample. One is to provide the sample with an excess nitrogen condition, and the other is to increase the pressure of the sample sintering. In this paper, the second option was chosen to sinter the powder of ε-Fe_2N. The XRD pattern of sintered ε-Fe_2N is exactly the same as that of unsintered ε-Fe_2N. The result proves that a higher pressure can effectively restrain the denitrogenation of ε-Fe_2N. The bulk ε-Fe_2N was successfully prepared at 8 GPa and 1273 K. This makes it possible to study the properties of bulk ε-Fe_2N.

The bulk ε-Fe_2N was polished for the Vickers hardness measurement. The result is shown in Figure 3. The determined

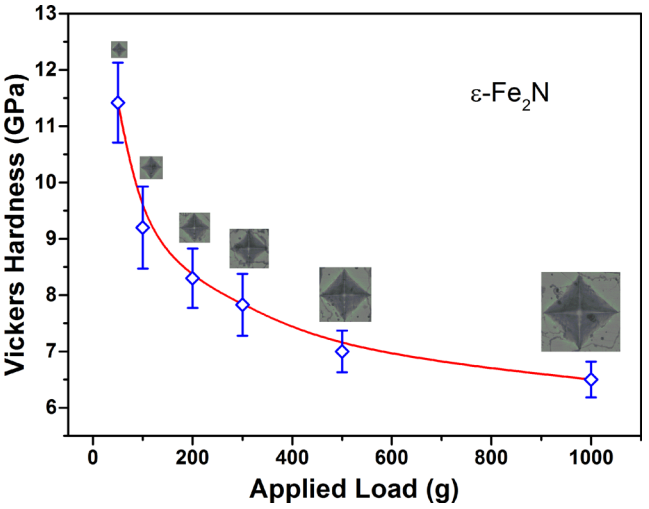

Figure 3. Vickers hardness of as-prepared ε-Fe_2N measured as a function of applied load ranging from 50 g (low load) to 1000 g (high load).

asymptotic hardness of ε-Fe_2N is about 6.5 GPa with a load of 1000 g. Under a same load (500 g), the hardness (7.1 GPa) of ε-Fe_2N is higher than that of ε-Fe_3N (5.9 GPa), which was reported by Yin et al. The hardness measurements suggest that ε-Fe_2N is not a hard material. According to the results reported in the literature, the Vickers hardness of Fe_2B is about 16 GPa.[44,45] Compared with Fe_2B, ε-Fe_2N has significantly lower hardness. Figure 1c shows the crystal structure of ε-Fe_2N. On comparing the crystal structures of Fe_2B and ε-Fe_2N, it can be found that there are many differences. The shortest Fe−Fe distance is 2.411 Å, the Fe−B distance is 2.169 Å, and the B−B distance is 2.127 Å in Fe_2B.[46] But in ε-Fe_2N, the Fe−Fe distance is 2.726 Å, the N−Fe distance is 1.941 Å, and the N−N distances are 2.764 and 3.539 Å. The N−N bond length is evidently longer than the B−B bond. In the crystal structure of ε-Fe_2N, the N atoms do not form spatial structures, which help improve the material hardness, like a three-dimensional mesh structure or a puckered quasi-three-dimensional (3D) structure, only two-dimensional results, and a part of the N atom is located at a position similar to the interstitial atom, completely surrounded by Fe atoms, so that no chemical bonds form with other N atoms. This makes the N atom has a limited effect on the hardness improvement of ε-Fe_2N. Fe_2N in other crystal structures may perform better in hardness, which needs further study and facilitates further understanding of the hardness mechanism.

Figure 4a displays the magnetic susceptibility curves of ε-Fe_2N. A ferromagnetic transition occurred in the sample within the temperature range (2−500 K). The measurement of ε-Fe_2N exhibited ferromagnetic behavior at relatively low temperature but paramagnetism at a higher temperature than room temperature. The Curie temperature T_c (~250 K) was evaluated by the field-cooled (FC) and zero-field-cooled (ZFC) data. Between 350 and 450 K, the temperature

https://doi.org/10.1021/acsomega.1c00551
ACS Omega 2021, 6, 12591−12597

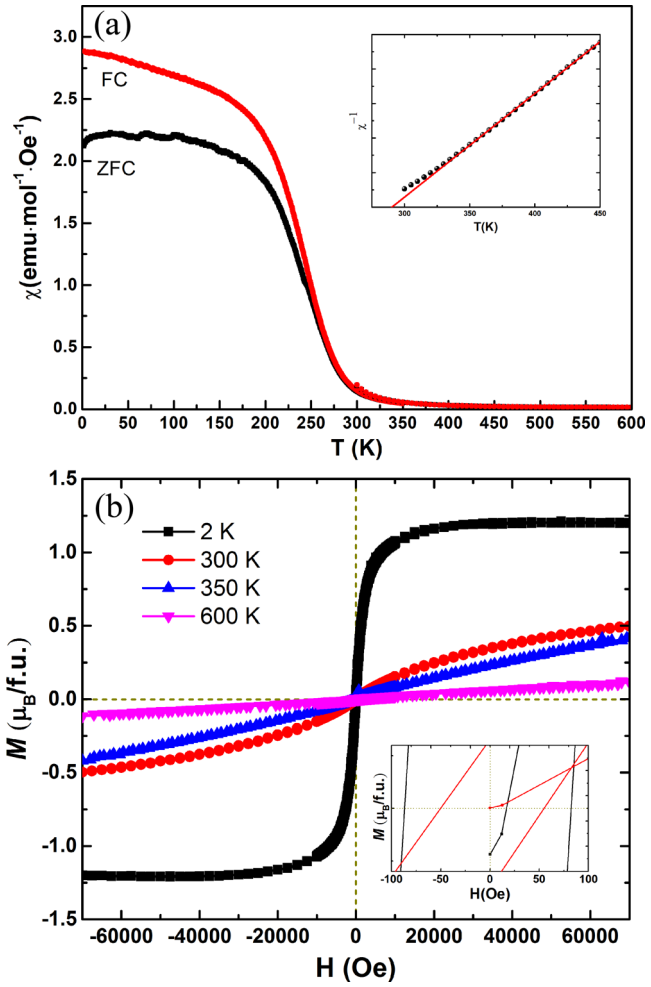

Figure 4. (a) Temperature dependence of zero-field-cooled (ZFC, black curve) and field-cooled (FC, red curve) magnetizations acquired under 1000 Oe field for evaluation of the blocking temperature and Curie temperature. The result of the Curie−Weiss fitting in 350−450 K is shown in the inset. (b) Isothermal hysteresis loops of ε-Fe_2N measured at the temperatures of 2, 300, 350, and 600 K. The inset shows the enlarged view of the magnetic hysteresis behavior at 2 and 300 K.

dependence of the reciprocal susceptibility is shown in the inset of Figure 4a. The Weiss constant (θ_w = 290.4 K) and the Curie constant (C = 3.33 (emu K)/(mol Oe)) can be obtained by fitting the reciprocal magnetic susceptibility with the Curie−Weiss law $\chi = C/(T - \theta_w)$. The effective magnetic moment (μ_{eff}) is calculated to be near 5.16 μ_B according to the Curie constant.

The field-dependent magnetization curves at 2, 300, 350, and 600 K were measured, and the hysteresis loops of ε-Fe_2N are shown in Figure 4b. The magnetization (M) versus magnetic field (H) curves of ε-Fe_2N suggest that the sample shows the linear magnetization behavior at higher temperatures like 350 K. At 300 K, the magnetic hysteresis loop slightly deviates from the linear magnetization behavior. The field-dependent magnetization was measured with the field swept from −70 to 70 KOe. At 2 K, it can be found that the magnetization reaches saturation with the magnetic field of ∼2 T and the saturation magnetization (M_s) is about 1.2 μ_B. The hysteresis loops hardly show any hysteretic behavior with nearly zero coercivity, Hc, which indicates that ε-Fe_2N may be a potential soft magnetic material.

In this paper, the electron transport of ε-Fe_2N was studied by a physical property measurement system (PPMS). The electrical resistivity (ρ) measurement was carried out in the temperature range between 2 and 300 K. The measured $\rho-T$ data is plotted in Figure 5a. In the measurement temperature

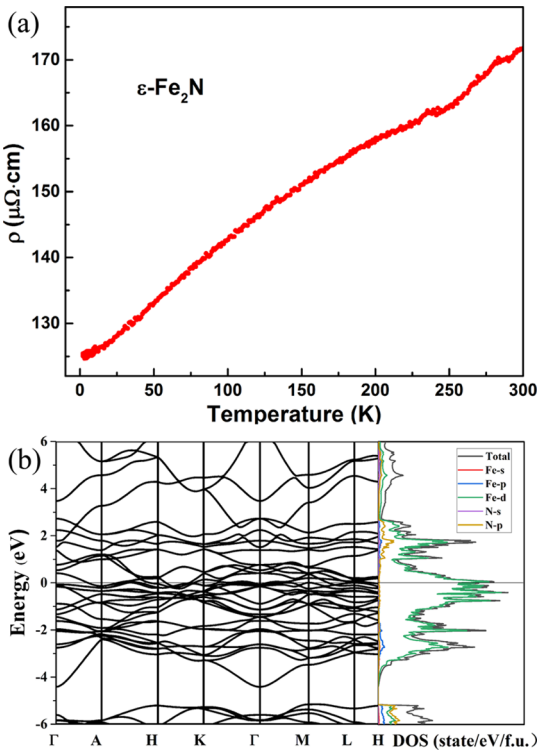

Figure 5. (a) Electrical resistivity measurement of ε-Fe_2N from 300 to 2 K. (b) Calculated electronic band structure (left panel) and projected density of states (PDOS) (right panel) of ε-Fe_2N.

range, the superconducting transition had not occurred in this compound. The room-temperature resistivity of ε-Fe_2N is small (172 $\mu\Omega$ cm) and close to that of the aluminum−nickel−iron alloy (160 $\mu\Omega$ cm), suggesting metal conductivity. The curve of the resistivity with the temperature is typical of metal behavior. This is further evidence that ε-Fe_2N has metal conductivity.

To better understand the electronic transport properties of ε-Fe_2N, the electronic band structure of ε-Fe_2N was calculated, as shown in Figure 5b. The projected density of states (PDOS) also shows that bulk ε-Fe_2N is a metallic conductor. The conducting states mainly derive from Fe-3d states around the Fermi level, and the valence band is mainly occupied by that. The other states, like N-2p states, make a quiet small contribution to the states near the Fermi level. This result is basically consistent with the previous calculation done by Matar et al.,[47] who used the augmented spherical wave (ASW) method.

CONCLUSIONS

In summary, we successfully prepared the bulk ε-Fe_2N. The powder ε-Fe_2N was synthesized via the SSM reaction under high pressures, high temperatures (HPHT) between $FeCl_2$ and Ca_3N_2. The bulk ε-Fe_2N was sintered under higher HPHT. The thermal stability of ε-Fe_2N was investigated by TG

https://doi.org/10.1021/acsomega.1c00551
ACS Omega 2021, 6, 12591−12597

analysis and differential scanning calorimetry (DSC). The measurement results show that the compound started to decompose at 670 K and was completely decomposed at 920 K. The Vickers hardness measurements suggest that the determined asymptotic hardness of ε-Fe_2N was about 6.5 GPa with a load of 1000 g. The magnetic property studies demonstrate that ε-Fe_2N is ferromagnetic, consistent with the literature report, but the T_C is different. In this study, the Curie temperature was about 250 K, the effective magnetic moment (μ_{eff}) was 5.26 μ_B, and the saturation magnetization (M_s) was 1.2 μ_B at 2 K. As an important part of the bulk properties, the electron transport of ε-Fe_2N was studied and proved to be a conductor. The resistivity of ε-Fe_2N is 172 $\mu\Omega$ cm at room temperature. The result of the calculation shows that the Fe-3d states make primarily contribution to the conducting states around the Fermi level.

EXPERIMENTAL SECTION

The ε-Fe_2N was prepared by a high-pressure solid-state metathesis (HPSSM) reaction between calcium nitride (Ca_3N_2) and ferrous chloride ($FeCl_2$). High-purity Ca_3N_2 (>99%, Alfa Aesar) and $FeCl_2$ (>99.9%, Alfa Aesar) powders in the molar ratio $Ca_3N_2/FeCl_2$ = 1:2.5 were homogeneously mixed and compacted into cylindrical pellets (6 mm in diameter and 4 mm in height) for the synthesis of iron nitrides. In each experimental run, the pellet was contained in a gold capsule to prevent potential contamination. The high-pressure synthesis experiments were performed in a cubic-anvil-type high-pressure apparatus. Figure 6 displays the process of preparing samples with the high-pressure apparatus. Under the condition of target pressure 5 GPa, the finely mixed reactants were quickly heated to 1073 K at a heating rate of 100 K/min and then quenched to room temperature after a duration time of 30 min. After the heat treatment, the pressure was slowly released. The products obtained from the high-pressure and high-temperature treatment were rinsed with deionized water to exclude the byproduct $CaCl_2$. The water-washed high-pressure product was compacted into cylindrical pellets (3 mm in diameter and 2 mm in height), which were contained in a gold capsule, for the preparation of the bulk ε-Fe_2N. The treatment of ε-Fe_2N was sintered at 8 GPa and 1273 K for a duration of about 30 min.

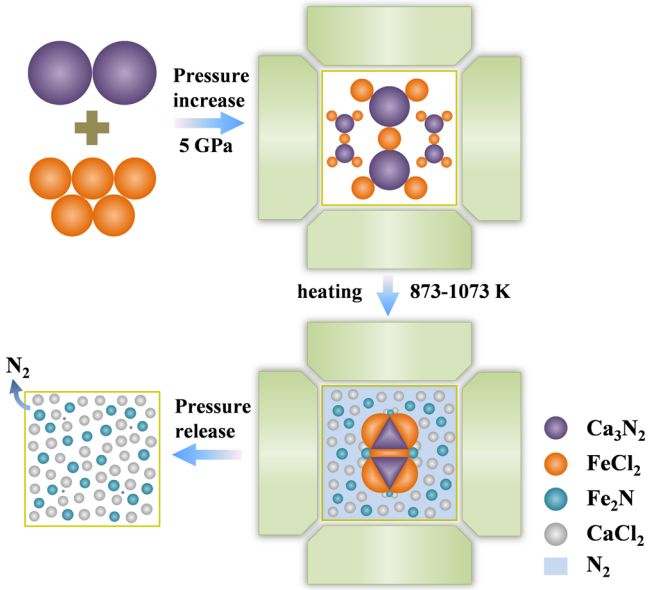

Figure 6. Reaction process for the formation of Fe_2N in high-pressure solid-state metathesis. Purple spheres/triangle, orange spheres/hemispheres, aqua spheres, and gray spheres represent Ca_3N_2, $FeCl_2$, Fe_2N, and $CaCl_2$, respectively. The light blue rectangle represents nitrogen.

The phase identification and structural characterization of the final products were performed by powder X-ray diffraction (Huber diffractometer, Germany) with Cu Kα radiation (λ = 1.5406 Å, 40 kV, 300 mA). The diffraction angle (2θ) ranges from 20 to 90° in steps of 0.005°. XRD data of the final products were refined with GSAS software based on the Rietveld method.[48] The asymptotic Vickers hardness of polished bulk samples was measured using a microhardness tester with a standard pyramid diamond indenter under different loads from 50 to 1000 g (50, 100, 200, 300, 500, 1000 g). To improve the fidelity of these measurements, hardness tests for the same load were repeated 10 times with a dwelling time of 15 s for each test. The final Vickers hardness for each load was obtained from the mean value of the 10 tests, and the error bar is the standard deviation of the 10 tests. Data of resistivity (ρ) were collected on a physical property measurement system (PPMS7, Quantum Design). Magnetic susceptibility and magnetization were measured on a superconducting quantum interference device magnetometer (MPMS3, Quantum Design). Thermogravimetric (TG) analysis measurements with room-temperature (RT) scan up to 1100 K were performed on a Setaram TG-DTA system. The powder samples were heated up to 1100 K at a rate of 5 K/min, soaked at the temperature of 1100 K for 5 min, and naturally cooled to room temperature in a mixture of hydrogen (4%) and argon (96%) atmosphere.

First-principles calculations were carried out using the plane-wave pseudopotential method, which was implemented in the Vienna ab Initio Simulation Package (VASP),[49] within the framework of density functional theory. The generalized gradient approximation (GGA) of Perdew–Burke–Ernzerhof[50] was utilized to determine the exchange–correlation term. The electron–ion interaction was described by projected augmented wave (PAW) potentials with $3d^64s^2$ and $2s^22p^3$ as valence electrons for Fe and N, respectively. A kinetic cutoff energy of 500 eV and a Monkhorst–Pack k mesh of 0.03 × 2π $Å^{-1}$ were chosen to ensure that enthalpy can converge to better than 1 meV/formula units (f.u.).

ASSOCIATED CONTENT

Supporting Information

The Supporting Information is available free of charge at https://pubs.acs.org/doi/10.1021/acsomega.1c00551.

Temperature dependence of differential thermal analysis; XRD pattern of the denitrogen at different temperatures; and crystal structure data for refinements in the space group $P6_322$ (PDF)

AUTHOR INFORMATION

Corresponding Authors

Fang Hong − *Beijing National Laboratory for Condensed Matter Physics, Institute of Physics Chinese Academy of Sciences, Beijing 100190, China*; Email: hongfang@iphy.ac.cn

https://doi.org/10.1021/acsomega.1c00551
ACS Omega 2021, 6, 12591−12597

Pinwen Zhu − *State Key Laboratory of Superhard Materials, College of Physics, Jilin University, Changchun 130012, China;* orcid.org/0000-0002-6357-5552; Email: zhupw@jlu.edu.cn

Xiaohui Yu − *Beijing National Laboratory for Condensed Matter Physics, Institute of Physics Chinese Academy of Sciences, Beijing 100190, China*; Email: yuxh@iphy.ac.cn

Authors

Teng Ma − *State Key Laboratory of Superhard Materials, College of Physics, Jilin University, Changchun 130012, China; Beijing National Laboratory for Condensed Matter Physics, Institute of Physics Chinese Academy of Sciences, Beijing 100190, China;* orcid.org/0000-0002-4057-7942

Yunyu Yin − *Beijing National Laboratory for Condensed Matter Physics, Institute of Physics Chinese Academy of Sciences, Beijing 100190, China*

Complete contact information is available at: https://pubs.acs.org/10.1021/acsomega.1c00551

Notes

The authors declare no competing financial interest.

■ ACKNOWLEDGMENTS

This work was supported by the National Key R&D Program of China under Grant nos. 2016YFA0401503 and 2018YFA0305700, the National Natural Science Foundation of China under Grant nos. 11575288 and 11974131, and the Youth Innovation Promotion Association of Chinese Academy of Sciences under Grant no. 2016006.

■ REFERENCES

(1) Calais, J.-L. Band structure of transition metal compounds. *Adv. Phys.* **1977**, *26*, 847−885.

(2) Neckel, A. Recent investigations on the electronic structure of the fourth and fifth group transition metal monocarbides, mononitrides, and monoxides. *Int. J. Quantum Chem.* **1983**, *23*, 1317−1353.

(3) Trudeau, M. L.; Schulz, R.; Dussault, D.; Van Neste, A. Structural changes during high-energy ball milling of iron-based amorphous alloys: Is high-energy ball milling equivalent to a thermal process? *Phys. Rev. Lett.* **1990**, *64*, 99−102.

(4) Pierson, H. O. *Handbook of Refractory Carbides and Nitrides*; Noyes Publications: Westwood, New Jersey, 1996.

(5) Salamat, A.; Hector, A. L.; Kroll, P.; McMillan, P. F. Nitrogen-rich transition metal nitrides. *Coord. Chem. Rev.* **2013**, *257*, 2063−2072.

(6) Fujiwara, Y.-i.; Lee, J.-S. M.; Tsujimoto, M.; Kongpatpanich, K.; Pila, T.; Iimura, K.-i.; Tobori, N.; Kitagawa, S.; Horike, S. Fabrication of ε-Fe_2N Catalytic Sites in Porous Carbons Derived from an Iron−Triazolate Crystal. *Chem. Mater.* **2018**, *30*, 1830−1834.

(7) Wei, Q.; Zhao, C.; Zhang, M.; Yan, H.; Wei, B. High-pressure phases and pressure-induced phase transition of MoN_6 and ReN_6. *Phys. Lett. A* **2019**, *383*, 2429−2435.

(8) Ye, T. N.; Park, S. W.; Lu, Y.; Li, J.; Sasase, M.; Kitano, M.; Hosono, H. Contribution of Nitrogen Vacancies to Ammonia Synthesis over Metal Nitride Catalysts. *J. Am. Chem. Soc.* **2020**, *142*, 14374−14383.

(9) Jack, K. H. Binary and ternary interstitial alloys I. The iron−nitrogen system: the structures of Fe_4N and Fe_2N. *Proc. R. Soc. London, Ser. A* **1948**, *195*, 34−40.

(10) Jack, K. H. The occurrence and the crystal structure of α''-iron nitride; a new type of interstitial alloy formed during the tempering of nitrogen-martensite. *Proc. R. Soc. London, Ser. A* **1951**, *208*, 216−224.

(11) Ortiz, C.; Dumpich, G.; Morrish, A. H. Epitaxial $Fe_{16}N_2$ films grown by sputtering. *Appl. Phys. Lett.* **1994**, *65*, 2737−2739.

(12) Dirba, I.; Komissinskiy, P.; Gutfleisch, O.; Alff, L. Increased magnetic moment induced by lattice expansion from α-Fe to α'-Fe_8N. *J. Appl. Phys.* **2015**, *117*, No. 173911.

(13) Shi, X.; Wu, M.; Lai, Z.; Li, X.; Gao, P.; Mi, W. Bending Strain-Tailored Magnetic and Electronic Transport Properties of Reactively Sputtered γ'-Fe4N/Muscovite Epitaxial Heterostructures toward Flexible Spintronics. *ACS Appl. Mater. Interfaces* **2020**, *12*, 27394−27404.

(14) Panda, R. N.; Gajbhiye, N. S. Magnetic properties of single domain ε-Fe_3N synthesized by borohydride reduction route. *J. Appl. Phys.* **1997**, *81*, 335−339.

(15) Minobe, S.; Nakajima, Y.; Hirose, K.; Ohishi, Y. Stability and compressibility of a new iron-nitride β-Fe_7N_3 to core pressures. *Geophys. Res. Lett.* **2015**, *42*, 5206−5211.

(16) Nagakura, S.; Tanehashi, K. Electronic Structure of Iron Nitrides Studied by Electron Diffraction. II. ε-Fe_2N and ζ-Fe_2N. *J. Phys. Soc. Jpn.* **1968**, *25*, 840−846.

(17) Hasegawa, M.; Yagi, T. Systematic study of formation and crystal structure of 3d-transition metal nitrides synthesized in a supercritical nitrogen fluid under 10 GPa and 1800 K using diamond anvil cell and YAG laser heating. *J. Alloys Compd.* **2005**, *403*, 131−142.

(18) Bykov, M.; Bykova, E.; Aprilis, G.; Glazyrin, K.; Koemets, E.; Chuvashova, I.; Kupenko, I.; McCammon, C.; Mezouar, M.; Prakapenka, V.; Liermann, H. P.; Tasnadi, F.; Ponomareva, A. V.; Abrikosov, I. A.; Dubrovinskaia, N.; Dubrovinsky, L. Fe−N system at high pressure reveals a compound featuring polymeric nitrogen chains. *Nat. Commun.* **2018**, *9*, No. 2756.

(19) Suzuki, K.; Morita, H.; Kaneko, T.; Yoshida, H.; Fujimori, H. Crystal structure and magnetic properties of the compound FeN. *J. Alloys Compd.* **1993**, *201*, 11−16.

(20) Suzuki, K.; Yamaguchi, Y.; Kaneko, T.; Yoshida, H.; Obi, Y.; Fujimori, H.; Morita, H. Neutron Diffraction Studies of the Compounds MnN and FeN. *J. Phys. Soc. Jpn.* **2001**, *70*, 1084−1089.

(21) Niwa, K.; Terabe, T.; Kato, D.; Takayama, S.; Kato, M.; Soda, K.; Hasegawa, M. Highly Coordinated Iron and Cobalt Nitrides Synthesized at High Pressures and High Temperatures. *Inorg. Chem.* **2017**, *56*, 6410−6418.

(22) Clark, W. P.; Steinberg, S.; Dronskowski, R.; McCammon, C.; Kupenko, I.; Bykov, M.; Dubrovinsky, L.; Akselrud, L. G.; Schwarz, U.; Niewa, R. High-Pressure NiAs-Type Modification of FeN. *Angew. Chem., Int. Ed.* **2017**, *56*, 7302−7306.

(23) Laniel, D.; Dewaele, A.; Garbarino, G. High Pressure and High Temperature Synthesis of the Iron Pernitride FeN_2. *Inorg. Chem.* **2018**, *57*, 6245−6251.

(24) Mekata, M.; Yoshimura, H.; Takaki, H. Magnetic Study on Hexagonal Nitrides of 3d Transition Metals. *J. Phys. Soc. Jpn.* **1972**, *33*, 62−69.

(25) Gerardin, D.; Morniroli, J. P.; Michel, H.; Gantois, M. Microstructural study of ε-iron-carbonitrides formed by a glow discharge technique. *J. Mater. Sci.* **1981**, *16*, 159−169.

(26) Hwang, J.-W.; Campbell, J. P.; Kozubowski, J.; Hanson, S. A.; Evans, J. F.; Gladfelter, W. L. Topochemical Control in the Solid-State Conversion of Cyclotrigallazane into Nanocrystalline Gallium Nitride. *Chem. Mater.* **1995**, *7*, 517−525.

(27) Houmes, J. D.; zur Loye, H.-C. Microwave Synthesis of Ternary Nitride Materials. *J. Solid State Chem.* **1997**, *130*, 266−271.

(28) Vaidhyanathan, B.; Rao, K. J. Synthesis of Ti, Ga, and V Nitrides: Microwave-Assisted Carbothermal Reduction and Nitridation. *Chem. Mater.* **1997**, *9*, 1196−1200.

(29) Wu, C.; Li, T.; Lei, L.; Hu, S.; Liu, Y.; Xie, Y. Indium nitride from indium iodide at low temperatures: synthesis and their optical properties. *New J. Chem.* **2005**, *29*, No. 1610.

(30) Mazumder, B.; Hector, A. L. Use of low temperature solvothermal reactions in the synthesis of nanocrystalline tantalum nitrides including nanorods. *J. Mater. Chem.* **2008**, *18*, No. 1392.

(31) Gillan, E. G.; Kaner, R. B. Rapid Solid-State Synthesis of Refractory Nitrides. *Inorg. Chem.* **1994**, *33*, 5693−5700.

(32) Hector, A. L.; Parkin, I. P. Sodium azide as a reagent for solid state metathesis preparations of refractory metal nitrides. *Polyhedron* **1995**, *14*, 913−917.
(33) Choi, J.; Gillan, E. G. Solvothermal metal azide decomposition routes to nanocrystalline metastable nickel, iron, and manganese nitrides. *Inorg. Chem.* **2009**, *48*, 4470−4477.
(34) Lei, L.; Yin, W.; Jiang, X.; Lin, S.; He, D. Synthetic route to metal nitrides: high-pressure solid-state metathesis reaction. *Inorg. Chem.* **2013**, *52*, 13356−62.
(35) Niewa, R.; Rau, D.; Wosylus, A.; Meier, K.; Hanfland, M.; Wessel, M.; Dronskowski, R.; Dzivenko, D. A.; Riedel, R.; Schwarz, U. High-Pressure, High-Temperature Single-Crystal Growth, Ab initio Electronic Structure Calculations, and Equation of State of ϵ-Fe_3N_{1+x}. *Chem. Mater.* **2009**, *21*, 392−398.
(36) Yin, W.; Lei, L.; Jiang, X.; Liu, P.; Liu, F.; Li, Y.; Peng, F.; He, D. High pressure synthesis and properties studies on spherical bulk ϵ-Fe_3N. *High Pressure Res.* **2014**, *34*, 317−326.
(37) Schwarz, U.; Wosylus, A.; Wessel, M.; Dronskowski, R.; Hanfland, M.; Rau, D.; Niewa, R. High-Pressure-High-Temperature Behavior of ζ-Fe_2N and Phase Transition to ϵ-$Fe_3N_{1.5}$. *Eur. J. Inorg. Chem.* **2009**, *2009*, 1634−1639.
(38) Lehmann, T. S.; Niewa, R. Electrochemical Synthesis of Highly Nitrogen Containing γ-$FeN_{0.13}$ and ϵ-$Fe_3N_{1.51}$ in a Molten Salt System. *Eur. J. Inorg. Chem.* **2019**, *2019*, 730−734.
(39) Leineweber, A.; Jacobs, H.; Hüning, F.; Lueken, H.; Kockelmann, W. Nitrogen ordering and ferromagnetic properties of ϵ-Fe_3N_{1+x} ($0.10 \leq x \leq 0.39$) and ϵ-$Fe_3(N_{0.80}C_{0.20})_{1.38}$. *J. Alloys Compd.* **2001**, *316*, 21−38.
(40) Serghiou, G.; Ji, G.; Odling, N.; Reichmann, H. J.; Frost, D. J.; Wright, J. P. Synthesis and high-resolution study distinguishing between very similar interstitial iron nitride structures. *High Pressure Res.* **2015**, *35*, 28−36.
(41) Leineweber, A.; Jacobs, H. Theoretical analysis of occupational ordering in hexagonal interstitial compounds: carbides, nitrides and oxides with "ϵ-type" superstructures. *J. Alloys Compd.* **2000**, *308*, 178−188.
(42) Jack, K. H. The iron−nitrogen system: the crystal structures of ϵ-phase iron nitrides. *Acta Cryst.* **1952**, *5*, 404−411.
(43) Jiang, Y.; Jiang, L. Synthesis of -Fe_4N Soft Magnetic Material by High-Pressure Nitriding Approach. *IEEE Trans. Magn.* **2019**, *55*, 1−4.
(44) Huang, Z.; Xing, J.; Guo, C. Improving fracture toughness and hardness of Fe_2B in high boron white cast iron by chromium addition. *Mater. Des.* **2010**, *31*, 3084−3089.
(45) Jian, Y.; Huang, Z.; Xing, J.; Guo, X.; Jiang, K. Effect of molybdenum addition on mechanical properties of oriented bulk Fe_2B crystal. *J. Mater. Res.* **2017**, *32*, 1718−1726.
(46) Kumar, P. A.; Satya, A.; Reddy, P. S.; Sekar, M.; Kanchana, V.; Vaitheeswaran, G.; Mani, A.; Kalavathi, S.; Shekar, N. C. Structural and low temperature transport properties of Fe_2B and FeB systems at high pressure. *J. Phys. Chem. Solids* **2017**, *109*, 18−25.
(47) Matar, S.; Mohn, P. Electronic And Magnetic Properties of Fe_2N and FeN: Trends of The Magnetism of The Fe−N Systems. *Act. Passive Electron. Compon.* **1993**, *15*, 89−101.
(48) Larson, A. C.; Dreele, R. B. V. *General Structure Analysis System (GSAS)*, Report No. LAUR 86-748; Los Alamos National Laboratory: Los Alamos, NM, 1994.
(49) Kresse, G.; Furthmuller, J. Efficient iterative schemes for ab initio total-energy calculations using a plane-wave basis set. *Phys. Rev. B* **1996**, *54*, 11169.
(50) Perdew, J. P.; Chevary, J. A.; Vosko, S. H.; Jackson, K. A.; Pederson, M. R.; Singh, D. J.; Fiolhais, C. Atoms, molecules, solids, and surfaces: Applications of the generalized gradient approximation for exchange and correlation. *Phys. Rev. B* **1992**, *46*, 6671−6681.

https://doi.org/10.1021/acsomega.1c00551
ACS Omega 2021, 6, 12591−12597